

Journal of Materials Chemistry A

Accepted Manuscript



This is an *Accepted Manuscript*, which has been through the Royal Society of Chemistry peer review process and has been accepted for publication.

Accepted Manuscripts are published online shortly after acceptance, before technical editing, formatting and proof reading. Using this free service, authors can make their results available to the community, in citable form, before we publish the edited article. We will replace this *Accepted Manuscript* with the edited and formatted *Advance Article* as soon as it is available.

You can find more information about *Accepted Manuscripts* in the [Information for Authors](#).

Please note that technical editing may introduce minor changes to the text and/or graphics, which may alter content. The journal's standard [Terms & Conditions](#) and the [Ethical guidelines](#) still apply. In no event shall the Royal Society of Chemistry be held responsible for any errors or omissions in this *Accepted Manuscript* or any consequences arising from the use of any information it contains.



www.rsc.org/materialsA

Superior Electric Double Layer Capacitors Using Micro- and Mesoporous Silicon Carbide Sphere

Cite this: DOI: 10.1039/x0xx00000x

Myeongjin Kim, Ilgeun Oh and Jooheon Kim*

Received 00th January 2012,
Accepted 00th January 2012

DOI: 10.1039/x0xx00000x

www.rsc.org/

Three-dimensional silicon carbide-based frameworks with hierarchical micro and mesoporous structures (MMPSiC) are prepared by employing the template method and carbonization reaction via the aerosol-spray drying method. The mesopores are generated by the self-assembly of a structure-directing agent, while the micropores are derived from the partial evaporation of Si atoms during the carbonization process. MMPSiC has a unique three-dimensionally interconnected micro and mesoporous network; it also exhibits a faster ion-transport behavior and a larger utilization of the surface area of the electric double-layer capacitors. MMPSiC shows a high-charge storage capacity, with a specific capacitance of 253.7 F g⁻¹ in 1 M Na₂SO₄ aqueous electrolyte at a scan rate of 5 mV s⁻¹. In addition, a specific capacitance of 40.3 F g⁻¹ is measured in the 3-ethyl-3-methylimidazolium bis(trifluorosulfonyl)imide ionic-liquid electrolyte at a scan rate of 5 mV s⁻¹, with an energy density of 68.56 Wh kg⁻¹; and ~98.4 % specific capacitance being retained over 20000 cycles. Such a high supercapacitor performance may arise from a synergistic effect ensured by the dual-pore system, which can provide a large accessible surface area for ion transport/charge storage by the mesopores and a continuous increase of charge accommodation by micropores. These encouraging results demonstrate the great potential of MMPSiC as high-performance electrode materials for supercapacitors.

1. Introduction

Electrical double-layer capacitors (EDLCs), also simply named as supercapacitors, are a class of energy-storage devices that store charges in an electric double layer formed through the physisorption of electrolyte ions onto porous electrode materials.¹⁻⁴ With a promising combination of features such as high-power density and excellent cycling stability, EDLCs find use in several applications, including high-power electronic devices and electric and hybrid-electric vehicles.⁵⁻⁷ However, in most of these applications, EDLCs suffer from a limited energy density, which is typically of the order of 4-5 Wh/kg for fully assembled cells—an order of magnitude lower than that of batteries.⁸ Extensive research has been conducted toward the improvement of their energy densities by (i) increasing the capacitance with high-surface area electrode materials, and (ii) broadening the operational voltage with electrolytes that possess high-potential windows.^{9,10}

In order to obtain a high surface area, porous carbonaceous materials such as activated carbon, carbide-derived carbons, ordered mesoporous carbons, and carbon aerogels have been studied as high-surface area electrodes for EDLCs.^{8,11-16} However, the low electrical conductivity of these materials may hinder the formation of a conductive network (which decreases the internal resistance of an electrode) and the application of electrostatic charges on the surface of the electrode (which form the electric double layer).¹⁷ To address these issues, a few new approaches have been proposed that make

use of semiconductors or cermet nanowires as EDLC electrode materials instead of traditional carbon-based materials. Various types of EDLC materials such as silicon nanowires, silicon carbide nanowires, titanium nitride nanowires, titanium dioxide nanotubes, and nanowires have attracted considerable interest because of their high surface area and excellent electrical conductivity.¹⁸⁻²³ Among these, silicon carbide, especially nanowire-type silicon carbide, is considered as a promising EDLC material owing to the high electron mobility and low band gap with high surface area. However, because the working materials are grown directly on the current collector, these nanowire structures are not ideal for the fabrication of hybrid composites consisting of metal oxide or conductive polymers and for application as macroscale supercapacitor electrodes.

Recent studies have shown the silicon carbide microsphere particles to have great potential as EDLC materials; however, the porous properties of these silicon carbide microsphere particles (such as surface area and pore volume) are not satisfactory, because of their non-porous structure; this results in a low capacitive performance, e.g., 72.4 F g⁻¹ at a scan rate of 10 mV s⁻¹ in Na₂SO₄ aqueous electrolyte.²⁴⁻²⁶ Thus, in order to obtain a high surface area, silicon carbide particles with a porous structure need to be developed. The most widely used porous carbon materials for EDLCs contain a large proportion of micropores (pore diameter < 2 nm), which are not always fully accessible to ions.²⁷ In addition, the small micropores are not easily wetted by the electrolyte, and the exposed surface of the micropores cannot be utilized for charge

storage. Moreover, even if the micropores were wetted by the electrolyte, the ionic motion in such small pores would be so slow that a high-rate capability would not be achieved. Therefore, the dual-pore system combined with mesopores, which provide the ion-transport pathways with a minimized resistance, can be expected to provide a favorable electrochemical environment to achieve a fast ion-transport and high-charge storage capability.²⁸⁻³⁰

Herein, we developed novel micro and mesoporous silicon carbide (MMPSiC) spheres by employing the template method and carbonization reaction via the aerosol-spray drying method. These dual-pore systems are expected to exhibit the advantages typical of each pore size producing a synergistic effect during the electrochemical charge-discharge process. The prepared MMPSiC exhibits a large specific surface area of 1713 m² g⁻¹ with excellent electrical conductivity (187.9 S cm⁻¹), which is a desirable property for EDLC electrode materials. Finally, we successfully assembled a two-electrode symmetrical supercapacitor with a Na₂SO₄ aqueous electrolyte and the 3-ethyl-3-methylimidazolium bis(trifluorosulfonyl)imide ([EMIM][TFSI]) ionic-liquid electrolyte. Electrochemical characterizations indicated that the supercapacitor with the aqueous electrolyte can be reversibly cycled between 0 and 1.6 V, exhibiting a specific capacitance of 61.6 F g⁻¹ at a scan rate of 5 mV s⁻¹. Furthermore, the supercapacitor with the ionic-liquid electrolyte can be operated between 0 and 3.5 V, showing a specific capacitance of 40.3 F g⁻¹ at a scan rate of 5 mV s⁻¹ with an energy density of 68.56 Wh kg⁻¹; ~98.4 % specific capacitance was retained after 20000 cycles. These properties ensured a performance that is clearly superior to other commercially available devices (<3 W h kg⁻¹). These encouraging results showed that the obtained MMPSiC materials have a great potential as supercapacitor electrodes ensuring a high energy and power density.

2. Experimental

2.1 Synthesis of Micro & Mesoporous Silicon Carbide (MMPSiC)

In a typical synthesis, 0.917 g of Si nanoparticles (of about 5 nm) was dispersed in 33 mL of D.I. water. Subsequently, 0.014 mL of hydrogen chloride (HCl), 43.3 mL of ethanol (C₂H₅OH), and 1.9742 g of C₁₆H₃₃(EO)₁₀ (Brij56) were added and stirred for 1 h. The resulting solution mixtures were ultrasonically sprayed with a home humidifier (60 MHz and 35 W). The droplets were carried by argon (Ar) gas (purity: 99.999%) at a flow rate of 100 sccm (standard cubic centimeter per minute) into a tubular reactor. The tubular reactor is separated by two segments, namely the drying zone and heating zone. The drying-zone tubular reactor (30 mm in diameter and 700 mm in length) was heated up to 150 °C; the heating-zone tubular reactor (30 mm in diameter and 1000 mm in length) was heated up to 1250 °C. At the entrance of the heating zone, C₂H₅OH was ultrasonically and carried by Ar gas at a flow rate of 60 sccm. The particles were recovered by filtration at the outlet of the heating-zone tubular reactor. After the reaction was terminated and the reactor was cooled to room temperature, the resulting products were exposed to air and heated to 600 °C for 4 h to eliminate the superfluous carbon. Finally, the SiO₂ layer adsorbed on the surface

of the MMPSiC particles was removed by treatment with hydrofluoric acid (HF). MMPSiC powder (10 g) was placed in 300 mL of 10% HF solution and stirred for 24 h. The sample was then leached with distilled water until the pH of the leaching water reached a value of 7–8.

2.2 Characterization Methods

X-ray diffraction (XRD) patterns were collected (New D8-Advance/Bruker-AXS) at a scan rate of 1° s⁻¹ within the 2θ range 5°–80° using CuK_{α1} radiation (0.154056 nm). The morphologies of the samples were observed using high-resolution transmission electron microscopy (HR-TEM, JEM-3010) and field-emission scanning electron microscopy (FE-SEM, SIGMA, Carl Zeiss). X-ray photoelectron spectroscopy (XPS) analysis was performed on a VGMicrotech ESCA2000 system using a spectrometer with a Mg K_α X-ray source (1253.6 eV) and a hemispherical analyzer. During the curve fitting, the Gaussian peak widths were constant in each spectrum. Nitrogen sorption analysis was carried out using an ASAP 2020 accelerated surface area and porosimetry instrument (Micromeritics), equipped with an automated surface area at 77 K, using Brunauer–Emmett–Teller (BET) calculations for the surface area. The pore-size distribution plots were recorded from the desorption branch of the isotherms based on the nonlocal density functional theory (DFT).

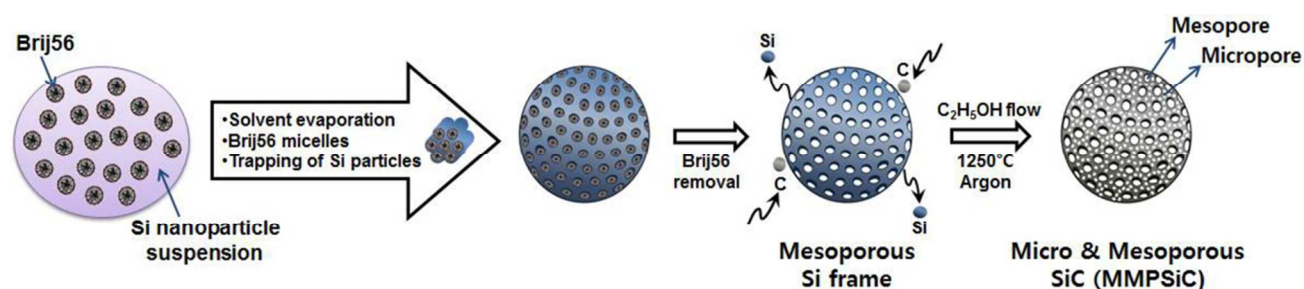
2.3 Preparation and Characterization of Supercapacitors

The working electrodes were fabricated as follows. First, the as-prepared materials, carbon black and poly(vinylidene fluoride) (PVDF) were mixed in a mass ratio of 85:10:5 and dispersed in *N*-methylpyrrolidone (NMP). The resulting mixture was then coated onto an aluminum foil substrate (1 cm × 1 cm) and dried in a vacuum oven at 60°C for 6 h. The loading mass of each electrode was approximately 3 mg. In a three-electrode cell, the above-loaded aluminum foil substrate, a platinum foil, and a Ag/AgCl (KCl-saturated) electrode were used as the working, counter, and reference electrodes, respectively. All measurements, including cyclic voltammetry (CV), galvanostatic charge/discharge characteristics, and Electrochemical impedance spectroscopy (EIS) measurements, were carried out on a CHI 660C electrochemical workstation in 1 M Na₂SO₄ aqueous solution at room temperature. EIS measurements were carried out by applying an AC voltage with 5 mV amplitude in a frequency range of 0.01 to 10⁵ Hz at open-circuit potential. For quantitative considerations, the specific capacitances (*C_s*) are calculated from the CV curves using the following equation :

$$C_s = \frac{1}{vM(V_c - V_a)} \int_a^c I(V) dV \quad (1)$$

where *C_s* is the specific capacitance (F g⁻¹), *v* is the potential scan rate (mV s⁻¹), *V_c* – *V_a* represents the sweep potential range (V), *M* is the weight of active materials in the working electrode (g) and *I(V)* denotes the response current density (A g⁻¹).

To construct symmetrical MMPSiC-based supercapacitor devices, the electrodes were prepared by same procedure mentioned above.



Scheme 1. Chemical route for the synthesis of MMPSiC.

The two symmetrical electrodes were separated using a celgard 2400 membrane in a CR2032 stainless steel coin cell. The CV, galvanostatic charge–discharge, and EIS tests for these devices were performed in both 1M Na₂SO₄ aqueous electrolyte and the 3-ethyl-3-methylimidazolium bis(trifluorosulfonyl)imide, [EMIM][TFSI] ionic liquid electrolyte. The specific capacitance of symmetrical MMPSiC-based supercapacitor was calculated from the Eq. (1). In case of the two electrode system, the specific capacitance was obtained using the total mass of active materials on the two electrodes. EIS was also performed in the frequency range of 0.01 to 10⁵ Hz at open circuit voltage with an alternate current amplitude of 5 mV. The equivalent series resistance (ESR) was estimated using the IR drop (V_{drop}) at a certain constant current density (I_{cons}) with the following equation:

$$R_{\text{ESR}} = \frac{V_{\text{drop}}}{2 \times I_{\text{cons}}} \quad (2)$$

The energy density and power density of symmetrical supercapacitor systems were calculated using the following equations:

$$E = \frac{1}{2} C (\Delta V)^2 \quad (3)$$

$$P = \frac{E}{t} \quad (4)$$

where P, C, ΔV , t, and E indicate the power density (W kg⁻¹), specific capacitance of the total symmetrical system (F g⁻¹), cell voltage for charging and discharging (V), discharge time (s), and energy density (Wh kg⁻¹), respectively.

3. Results and Discussion

Scheme 1 illustrates a schematic diagram for the preparation of the MMPSiC spheres. The solution mixtures of Brij56 and aqueous suspension of small Si particles (about 5 nm) are ultrasonically sprayed into a tubular reactor with two different reactor-temperature segments, namely the drying zone (150 °C) and the heating zone (1250 °C). At the threshold of the heating zone, C₂H₅OH, which was used as a carbon source, was sprayed and carried by Ar gas. In the drying zone, when the solvent evaporates from the solution mixtures, Brij56 form micellar rods and self-assemble into a hexagonal array, and then the Si particles are trapped in the voids of the Brij56 micellar rod, leading to formation of Si walls.^{31–33} In the heating zone, the Brij56 micelles are removed, resulting in the formation of

ordered hexagonal arrangement of mesopores, and then the resulting mesoporous Si sphere frames are converted to micro & mesoporous SiC spheres by the carbonization using C₂H₅OH as the carbon source.³⁴

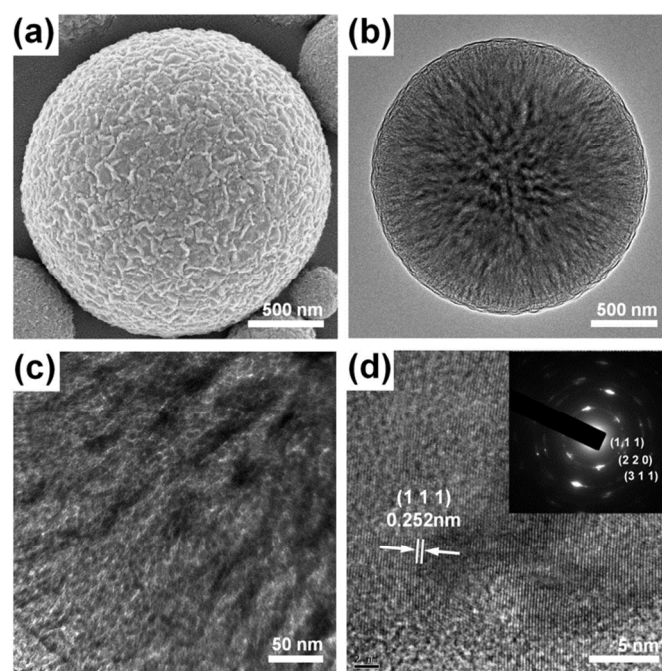


Figure 1. (a) FE-SEM image of MMPSiC. (b) FE-TEM image of MMPSiC. (c,d) High-magnification FE-TEM image of MMPSiC and SAED pattern (inset in (d)).

The SEM image in Figure 1(a) and S1 shows that the diameter of the MMPSiC particles prepared by the aerosol-spray drying method ranges between 1 and 3 μm ; the image confirmed that the particles have a spherical morphology. The HR-TEM analysis of the MMPSiC particles (Figures 1(b) and (c)) clearly shows disordered mesopores and channels. The hexagonally aligned mesopores in the Si sphere frames are collapsed and integrated with neighboring mesopores during the carbonization process due to the partial evaporation of Si atoms in the walls of the ordered mesopores. Furthermore, Figure 1(d) reveals that a large fraction of the micropores of the MMPSiC particles is randomly orientated. The formation of the micropores on mesoporous SiC can be attributed to a partial evaporation of the Si atoms from the mesoporous Si sphere

frames and carbonization of the remaining micro and mesoporous Si sphere frames at high temperature. At the heating temperature of 1250 °C, some of the Si atoms are released from the mesoporous Si sphere frames, forming micropores; this in turn leads to the formation of micro and mesoporous Si sphere frames. At the same time, the remaining micro and mesoporous Si sphere frames react with active-carbon species decomposed from C₂H₅OH to form micro and mesoporous SiC spheres. After carbonization, the mother mesoporous Si spheres were completely converted into micro and mesoporous SiC spheres.³⁴ These micro-mesoporous structures with a three-dimensional interconnection of MMPSiC can be expected to provide a favorable path for the transportation and penetration of electrolyte ions, which are both critical for a fast ion transfer.³⁵ In order to confirm the successful conversion of silicon carbide, the crystalline structure of MMPSiC was investigated. Figure 1(d) shows a typical HR-TEM image in which the lattice structures of MMPSiC are evident. The lattice interlayer distance is 0.252 ± 0.01 nm with a (1 1 1) spacing of β -SiC.³⁶ The inset of Figure 1(d) illustrates the selected-area electron diffraction (SAED) pattern of the shells with three clear diffraction rings, which correspond to the (1 1 1), (2 2 0), and (3 1 1) diffraction planes of β -SiC; this provides further evidence that the converted MMPSiC consists of well-crystallized β -SiC nanocrystals.³⁷

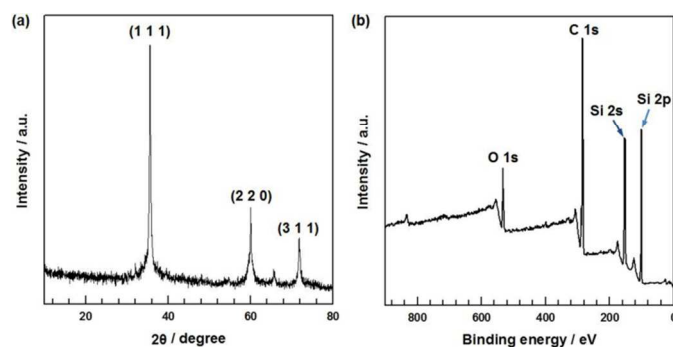


Figure 2. (a) XRD pattern of MMPSiC. (b) XPS wide scan survey spectra of MMPSiC.

XRD and XPS analyses were performed to verify the crystalline structure and chemical compositions of MMPSiC. The XRD pattern of Si nanoparticle as starting material shows distinct Si peaks at 28.4°, 47.2°, 56° and 68.9° corresponding to the (1 1 1), (2 2 0), (3 1 1) and (4 0 0) planes, respectively (JCPDS 01-0787) (Figure S2). Interestingly, after carbonization reaction, the XRD pattern of MMPSiC shows three β -SiC peaks at $2\theta = 35.6^\circ$, 60° , and 71.7° , which were assigned to the (1 1 1), (2 2 0), and (3 1 1) reflections, respectively; these indicate a face-centered cubic (fcc) β -SiC structure in accordance with the reference data (JCPDS 29-1129, $a = 4.3589$ Å) (Figure 2(a)).^{36,37} These XRD results are consistent with those obtained with TEM and SAED. The electrical conductivity of MMPSiC was determined to be 187.9 S cm^{-1} for pressed pellets using the four-point probe method. The excellent electrical conductivity of MMPSiC can be attributed to its β -polytype crystalline structure. It is well known that the β -polytype structure of SiC exhibits the highest electronic conductivity among the SiC polytypes, because β -SiC possesses the smallest band gap (~ 2.4 eV)

and one of the highest electron mobilities ($\sim 800 \text{ cm}^2 \text{ V}^{-1} \text{ s}^{-1}$ in low-doped material).³⁸ The XPS survey spectrum of the MMPSiC in Figure 2(b) reveals that MMPSiC consists of only three elements, namely C, Si, and O. To obtain detailed surface information of MMPSiC, the Si 2p and C 1s core-level spectra were deconvoluted (see Figure S3, Table S1 and S2 in ESI). The Si 2p region of the spectrum of MMPSiC (Figure S3(a)) shows that, besides a strong Si–C peak at the binding energy of 99.51 eV, some intermediate oxidation products of SiC (SiOC₃ at 100.42 eV, SiO₂C₂ at 101.31 eV, and SiO_xC at 102.2 eV) also exist on the surface.³⁹ The C 1s core level (Figure S3(b)) shows strong binding energy peaks of Si–C bonds at 282.72 eV, and C–C bonds at 284.61 eV, along with several binding energy peaks of SiO_xC_y at 283.68 eV.⁴⁰ The peak area ratio of Si–C/SiO_xC_y calculated from Si 2p spectra is 2.43, which shows good agreement with Si–C/SiO_xC_y ratio obtained from C 1s spectrum (2.46).

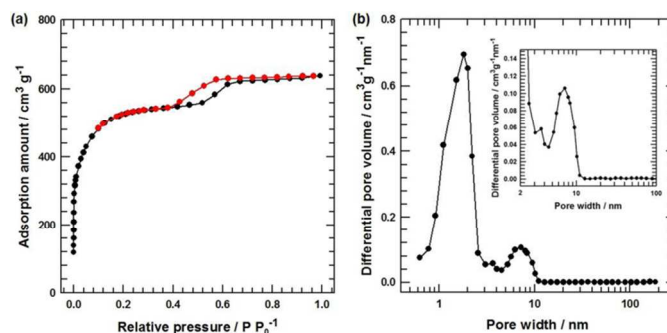


Figure 3. (a) Nitrogen adsorption-desorption isotherm of MMPSiC. (b) Pore size distribution of MMPSiC. (the inset illustrates mesopore region of MMPSiC)

The porous properties of the electrode materials are the crucial factor that determines the electrochemical performance of a supercapacitor. The BET and DFT analyses were employed to investigate the surface area and pore structure of MMPSiC and the results are shown in Figure 3. The nitrogen adsorption and desorption isotherm of MMPSiC is shown in Figure 3(a). The adsorption amount increases sharply at low relative pressures (P/P_0), demonstrating the existence of micropores; a hysteresis loop after $P/P_0 = 0.4$ can be observed, with an adsorption plateau near $P/P_0 = 1.0$; this indicates the presence of mesopores.²⁷ The total specific surface area of MMPSiC is calculated to be above $1713 \text{ m}^2 \text{ g}^{-1}$, with micropore and mesopore surface areas of $1372 \text{ m}^2 \text{ g}^{-1}$ and $341 \text{ m}^2 \text{ g}^{-1}$, respectively. The pore-size distribution of MMPSiC displayed in Figure 3(b) shows that its nanopores can be divided into two major regions: (i) micropores (< 2 nm) with a clear peak at 1.8 nm; (ii) mesopores (2–50 nm) with a maximum peak at 7.21 nm. According to the DFT calculation, the total, micropore, and mesopore volumes are $1.233 \text{ cm}^3 \text{ g}^{-1}$, $0.618 \text{ cm}^3 \text{ g}^{-1}$, and $0.615 \text{ cm}^3 \text{ g}^{-1}$, respectively. The assembly of micro and mesopores forms a hierarchical construction that provides the space for electric double layers and easy access channels for the electrolyte ions to the exterior and interior pore surfaces.⁴¹

The performance of the MMPSiC materials as supercapacitor electrodes was tested with CV, galvanostatic charge/discharge and EIS. In particular, Figure 4(a) and S4(a) show the CV curves of the

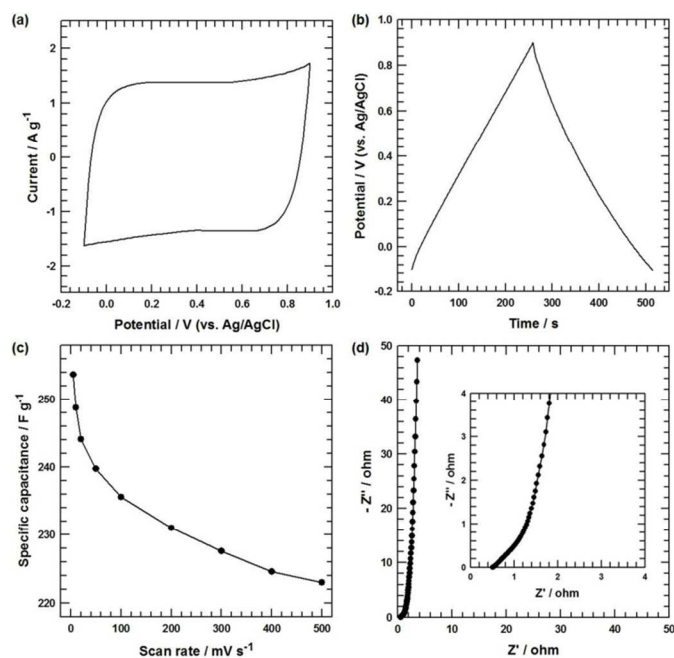


Figure 4. Electrochemical performance of MMPSiC electrode by three-electrode configuration. (a) CV curve of MMPSiC electrode at a scan rate of 5 mV s^{-1} . (b) Galvanostatic charge/discharge curve of MMPSiC electrode at a current density of 1 A g^{-1} . (c) Specific capacitance of MMPSiC electrode at different scan rates. (d) Nyquist plot of MMPSiC electrode. Inset magnifies the data in the high-frequency range.

MMPSiC electrode at various scan rate, with potential windows ranging between -0.1 and 0.9 V (vs. Ag/AgCl) in $1 \text{ M Na}_2\text{SO}_4$ aqueous solution. The CV curve has an almost ideally rectangular shape, without clear redox peaks, which indicates an ideal capacitive behavior of MMPSiC.⁴² Figure 4(b) displays the galvanostatic charge/discharge curve of the MMPSiC electrode measured between -0.1 and 0.9 V at a current density of 1 A g^{-1} in $1 \text{ M Na}_2\text{SO}_4$ aqueous electrolyte. During the charging and discharging steps, the charge curve of the MMPSiC electrode is almost symmetric to its corresponding discharge counterpart, revealing an electric double-layer contribution due to the connective porous structure. In order to obtain more information about the capacitive performance, the MMPSiC electrode was further analyzed. Figure S4(b) displays the galvanostatic charge/discharge curves of the MMPSiC electrode at different current densities; the curves become highly linear and symmetric as the current density increases. This implies that the MMPSiC electrode has an excellent electrochemical reversibility and charge-discharge properties.⁴³ Moreover, the IR drop is similar and not obvious on all curves, even at 10 A g^{-1} , indicating little overall resistance and excellent capacitive properties of the EDLC materials.⁴⁴ The specific capacitances were calculated from the CV curves according to Eq. (1); Figure 4(c) displays the relationship between the specific capacitance and the scan rate of the MMPSiC electrode. In particular, the MMPSiC electrode shows a specific capacitance of 253.7 F g^{-1} at a scan rate of 5 mV s^{-1} . The outstanding electrochemical performance of MMPSiC can be explained as following: (i) The mesopores of MMPSiC provide low-resistant

pathways for ion diffusion in the pores and a good charge propagation; this leads to an improved electrochemical performance. (ii) The abundant micropores play an essential role for the optimization of the electric double-layer surfaces, thereby leading to an improved capacitance. (iii) The high surface area and pore volume of MMPSiC, which stem from the dual-pore system (micro/mesoporous), are favorable features that provide the electrochemically surface area required for charge accumulation, facilitating the transport of electrolyte ions; this improves remarkably the overall electrochemical performance. (iv) The excellent electrical conductivity of MMPSiC can significantly decrease the internal resistance of an electrode by the formation of a conductive network and can facilitate the application of electrostatic charges, which favor the accumulation of the electric double layers.²⁷⁻³⁰ The Nyquist plot of MMPSiC (Figure 4(d)) shows an almost vertical line, which suggests a dominance of the double layer charge-storage at low frequencies.^{10,45} The inset in Figure 4(d) shows a magnified high-frequency range for MMPSiC. Diffusion control dominates when a phase shift of 45° is the typical feature for porous electrodes with respect to the Warburg impedance in the middle frequency range. Crucial parameters such as wettability, thickness, and porosity for the diffusion of ions into the bulk through the porous network of the electrode act on this phase.³⁵ The MMPSiC electrode shows negligible Warburg region on the Nyquist plots, which can be ascribed to the short and equal diffusion-path length of the ions in the aqueous electrolyte.

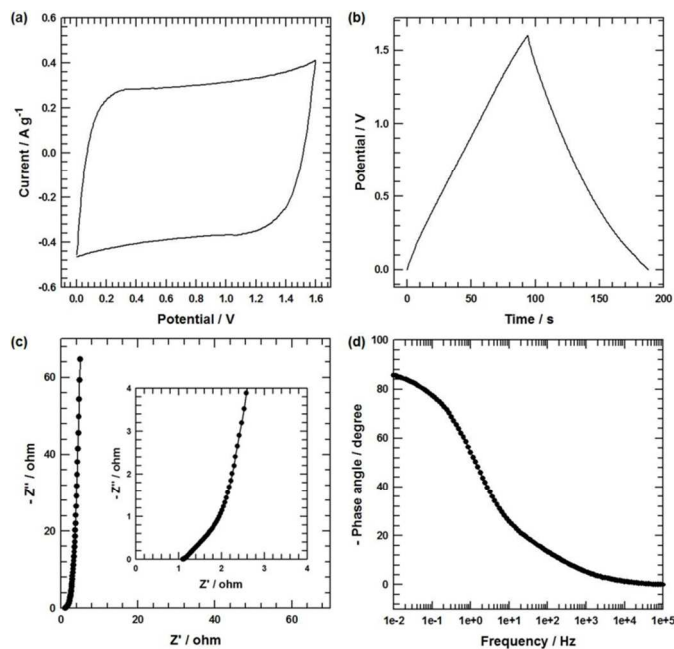


Figure 5. Electrochemical performance of two-electrode supercapacitors based on MMPSiC electrodes with $1 \text{ M Na}_2\text{SO}_4$ aqueous electrolyte. (a) CV curve of two-electrode supercapacitors at a scan rate of 5 mV s^{-1} . (b) Galvanostatic charge/discharge curve of two-electrode supercapacitors at a current density of 1 A g^{-1} . (c) Nyquist plot of two-electrode supercapacitors. Inset magnifies the data in the high-frequency range. (d) Impedance phase angle versus frequency.

CV, galvanostatic charge/discharge, and EIS spectra of the MMPSiC-based symmetrical two-electrode system in a 1 M Na₂SO₄ aqueous electrolyte were recorded. The CV curve of MMPSiC exhibits an ideal capacitive behavior with nearly a rectangular shape even at a potential window up to 1.6 V, implying fast dynamics and good charge propagation (Figure 5(a) and S5(a)). The charge-discharge curves (Figures 5(b) and S5(b)) at different current densities show good linear relationship between charge-discharge potentials and time, indicating a rapid I-V response and ideal capacitive characteristics.⁴⁶ From the CV curves, the specific capacitance (Figure S5(c)) was calculated as 61.6 F g⁻¹ at a scan rate of 5 mV s⁻¹. Moreover, the specific capacitance of the MMPSiC-based symmetric supercapacitor decreased from 61.6 F g⁻¹ (at 5 mV s⁻¹) to 52.1 F g⁻¹ (at 500 mV s⁻¹), this confirming an excellent capacitance retention (84.7%). These results indicate that the β-polytype crystal structure of MMPSiC plays an important role in providing a rapid charging-discharging capability, because a high electrical conductivity is an essential property of electrode materials when a supercapacitor works at high charging/discharging rates.²⁵ The almost vertical line in the low-frequency region demonstrates good capacitive behavior without diffusion limitations (Figure 5(c)). As shown in the inset in Figure 5(c), the intercept of the real axis in the high-frequency range of the symmetrical two-electrode system in the 1M Na₂SO₄ aqueous electrolyte (1.1 Ω) is significantly higher than that of the three-electrode configuration (0.49 Ω in Figure 4(d)), due to the additional contact resistance of the separator between the two electrodes.²⁵ Furthermore, at high-frequency regions, the phase angle is almost zero. In the middle region, a constant increase of the phase angle is observed as the frequency decreases. The phase angle shifts to negative values, reaching a value of -85.1° in the low-frequency limitation region, which is close to the value of an ideal capacitor (-90°) (Figure 5(d)).

The electrochemical performance of the MMPSiC-based supercapacitors was evaluated in a fully assembled two-electrode cell with the [EMIM][TFSI] ionic-liquid electrolyte. The CV profile was obtained for the voltage sweeps from 0 to 3.5 V (Figure 6(a)) with a scan rate of 5 mV s⁻¹. It can be seen that the CV curve of MMPSiC-based supercapacitor deviates from the ideal rectangular shape. Moreover, as shown in Figure S6(a), the shape of CV curve gradually transforms to oval shape with increasing scan rate. This phenomenon is caused by the poor compatibility and ionic conductivity of the organic electrolyte.^{35,41} The typical galvanostatic charge/discharge curves (Figure S6(b) in ESI) of the symmetrical supercapacitor at various current densities show slight curvature in discharge curves to their corresponding charge counterparts due to the poor electrochemical activity of organic electrolyte, which was confirmed by the CV curve behavior. Figure S6(c) shows the specific capacitances of symmetrical supercapacitors as a function of scan rates. The specific capacitance of a symmetrical supercapacitor was calculated as 40.3 F g⁻¹ at a scan rate of 5 mV s⁻¹. However, the capacitive performance in the organic electrolyte is poorer than that in the aqueous electrolyte due to the poor compatibility and ionic conductivity of the organic electrolyte; this was further investigated with the EIS analysis. In a comparison of the Nyquist plot of the organic electrolyte (Figure 6(b)) and aqueous electrolyte, the magnified high-to-medium-frequency region shows major

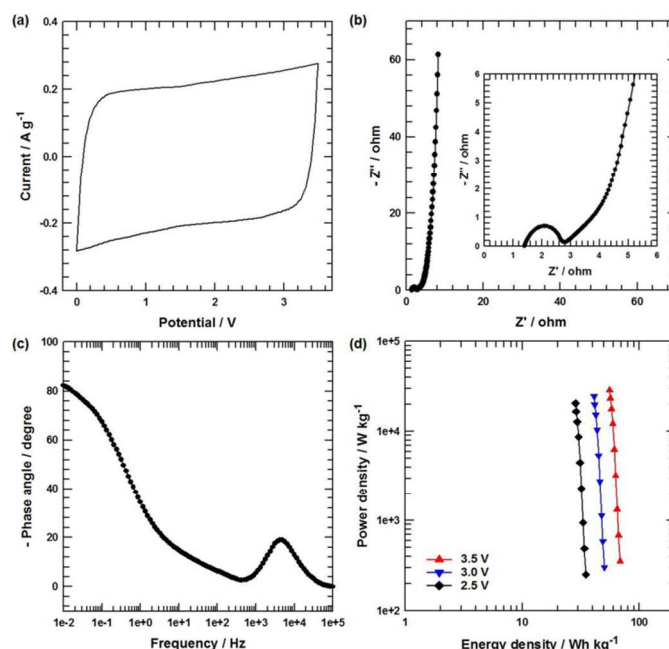


Figure 6. Electrochemical performance of two-electrode supercapacitors based on MMPSiC electrodes with 3-ethyl-3-methylimidazolium bis(trifluorosulfonyl)imide, [EMIM][TFSI] ionic liquid electrolyte. (a) CV curve of two-electrode supercapacitors at a scan rate of 5 mV s⁻¹. (b) Nyquist plot of two-electrode supercapacitors. Inset magnifies the data in the high-frequency range. (c) Impedance phase angle versus frequency. (d) Ragone plot of two-electrode supercapacitors as a function of cell operating voltage.

differences. The emergence of semicircle indicates a lower ionic conductivity of the organic electrolyte, and the relatively longer length of the 45° phase shift segment implies a higher Warburg impedance.^{35,41} Furthermore, the phase angle of the organic electrolyte (Figure 6 (c)) in the lower-frequency-limitation region is -82.2°, significantly lower than that of the aqueous electrolyte (-85.1°), indicating slower ion diffusion in the electrolyte and slower ion adsorption onto the electrode surface.⁴⁷ The poor compatibility between the active materials and the organic electrolyte prevented the electrolyte from adequately accessing the external surface and inner volume of MMPSiC, which resulted in limited outer-surface accessibility. The shift of the Nyquist plot towards the real axis is due to the ESR value of 2.73 Ω; this is in good agreement with the findings obtained from the IR drop observed in galvanostatic charge/discharge curves (Figure S6(b)).^{25,48} The cycling test of the cells also shows ~98.4 % capacitance retention over 20000 cycles at a current density of 10 A g⁻¹, indicating a good stability of the cell (Figure S6(d)). The Ragone plot for the symmetrical MMPSiC-based device at different scan rates is shown in Figure 6(d). At a low scan rate of 5 mV s⁻¹, the power and energy density values were found to be 352.67 W kg⁻¹ and 68.56 W h kg⁻¹, respectively, in a voltage window of 0 - 3.5 V, which is superior to commercial devices (<3 W h kg⁻¹).⁴⁹ It should be noted that the applied energy/power densities of the cell can be controlled to some extent by selecting a suitable working voltage to satisfy practical requirements.⁵⁰ These

encouraging results demonstrate that MMPSiC can be considered as a promising new EDLC material for supercapacitors, opening up new possibilities for the fabrication of improved porous-inorganic materials for energy-storage devices.

4. Conclusion

In summary, MMPSiC spheres were synthesized employing the template method and carbonization reaction via the aerosol spray-drying method. The MMPSiC electrode exhibits high-charge storage capacity, with a specific capacitance of 253.7 F g⁻¹ at a scan rate of 5 mV s⁻¹ with performance rate of 87.9 %, from 5 to 500 mV s⁻¹ in 1 M Na₂SO₄ aqueous electrolyte. In addition, a specific capacitance of 40.3 F g⁻¹ is obtained in the [EMIM][TFSI] ionic-liquid electrolyte at a scan rate of 5 mV s⁻¹. Such a high supercapacitor performance can be attributed to the high electric double-layer contribution ensured by the micro/mesoporosity, with a high effective surface area and excellent electrical conductivity of the conductive network.

Acknowledgements

This research was supported by Global Ph.D. Fellowship Program through the National Research Foundation of Korea (NRF) funded by the Ministry of Education (2014H1A2A1021380).

Notes and references

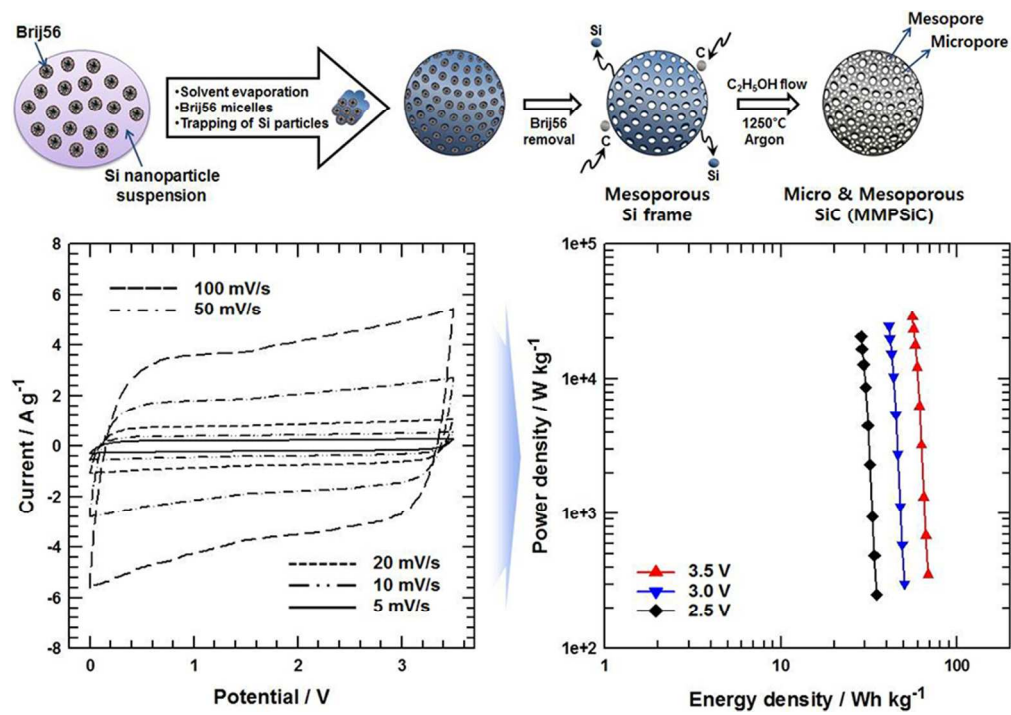
School of Chemical Engineering & Materials Science, Chung-Ang University, 84 Heukseok-Ro, Dongjak-gu, Seoul 156-756, Korea.

E-mail : jooheonkim@cau.ac.kr

Phone : +82-2-820-5763, Fax : +82-2-824-3495

- V. Subramanian, H. Zhu, R. Vajtai, P.M. Ajayan and B. Wei, *J. Phys. Chem. B.*, 2005, **109**, 20207-20214.
- A.L. Mohana, R.F. Estaline, A. Imran and J.S. Ramaprabhu, *Nanoscale Res. Lett.*, 2008, **3**, 145-151.
- A.C.-G. Karina, L.-C. Monica, C.-P. Nieves and G.-R. Pedro, *Adv. Funct. Mater.*, 2005, **15**, 1125-1133.
- J. Chow, R.J. Kopp and P.R. Portney, *Science*, 2003, **302**, 1528-1531.
- Z. Wen, X. Wang, S. Mao, Z. Bo, H. Kim, S. Cui, G. Lu, X. Feng and J. Chen, *Adv. Mater.*, 2012, **24**, 5610-5616.
- R. Kotz and M. Carlen, *Electrochim. Acta*, 2000, **45**, 2483-2498.
- Z. Chen, Y. Qin, D. Weng, Q. Xiao, Y. Peng, X. Wang, H. Li, F. Wei and Y. Lu, *Adv. Funct. Mater.*, 2009, **19**, 3420-3426.
- A. Burke, *Electrochim. Acta*, 2007, **53**, 1083-1091.
- M. Armand, F. Endres, D. R. MacFarlane, H. Ohno and B. Scrosati, *Nat. Mater.* 2009, **8**, 621-629.
- T. Kim, G. Jung, S. Yoo, K.S. Suh and R.S. Ruoff, *ACS Nano*, 2013, **7**, 6899-6905.
- J. Chmiola, G. Yushin, Y. Gogotsi, C. Portet, P. Simon and P. L. Taberna, *Science*, 2006, **313**, 1760-1763.
- C. Portet, M. A. Lillo-Rodenas, A. Linares-Solano and Y. Gogotsi, *Phys. Chem. Chem. Phys.* 2009, **11**, 4943-4945.
- R. Dash, J. Chmiola, G. Yushin, Y. Gogotsi, G. Laudisio, J. Singer, J. Fischer and S. Kucheyev, *Carbon*, 2006, **44**, 2489-2497.
- W. Xing, S. Z. Qiao, R. G. Ding, F. Li, G. Q. Lu, Z. F. Yan and H. M. Cheng, *Carbon*, 2006, **44**, 216-224.
- K. Jurewicz, C. Vix-Guterl, E. Frackowiak, S. Saadallah, A. Reda, J. Parmentier, J. Patarin and F. Beguin, *J. Phys. Chem. Solids*. 2004, **65**, 287-293.
- R. W. Pekala, J. C. Farmer, C. T. Alviso, T. D. Tran, S. T. Mayer, J. M. Miller and B. Dunn, *J. Non-Cryst. Solids* 1998, **225**, 74-80.
- L.L. Zhang, R. Zhou and X.S. Zhao, *J. Mater. Chem.* 2010, **20**, 5983-5992.
- J.W. Choi, J. McDonough, S. Jeong, J.S. Yoo, C.K. Chan and Y. Cui, *Nano Lett.*, 2010, **10**, 1409-1413.
- J.P. Alper, M. Vincent, C. Carraro and R. Maboudian, *Appl. Phys. Lett.*, 2012, **100**, 163901-163904.
- J.P. Alper, M.S. Kim, M. Vincent, B. Hsia, V. Radmilovic, C. Carraro and R. Maboudian, *J. Power Sources*, 2013, **230**, 298-302.
- X. Lu, G. Wang, T. Zhai, M. Yu, S. Xie, Y. Ling, C. Liang, Y. Tong and Y. Li, *Nano Lett.*, 2012, **12**, 5376-5381.
- X. Lu, G. Wang, T. Zhai, M. Yu, J. Gan, Y. Tong and Y. Li, *Nano Lett.* 2012, **12**, 1690-1696.
- H. Zhang, T. Zhai, M. Yu, S. Xie, C. Liang, W. Zhao, S.C.I. Wang, Z. Zhang and X. Lu, *J. Mater. Chem. C*, 2013, **1**, 225-229.
- M. J. Kim, Y. J. Yoo and J. H. Kim, *J. Power Sources*, 2014, **265**, 214-222.
- M. J. Kim and J. H. Kim, *Phys. Chem. Chem. Phys.* 2014, **16**, 11323-11336.
- M. J. Kim and J. H. Kim, *ACS Appl. Mater. Interfaces*. 2014, **6**, 9036-9045.
- F. Xu, R. Cai, Q. Zeng, C. Zou, D. Wu, F. Li, X. Lu, Y. Liang and R. Fu, *J. Mater. Chem.*, 2011, **21**, 1970-1976.
- Z.S. Wu, Y. Sun, Y.Z. Tan, S. Yang, X. Feng and K. Mullen, *J. Am. Chem. Soc.* 2012, **134**, 19532-19535.
- D.W. Wang, F. Li, M. Liu, G.Q. Lu and H.M. Cheng, *Angew. Chem. Int. Ed.* 2008, **47**, 373-376.
- W. Xiong, M. Liu, L. Gan, Y. Lv, Z. Xu, Z. Hao and L. Chen, *Colloids and Surfaces A: Physicochem. Eng. Aspects* 2012, **411**, 34-39.
- Z.Y. Yuan and B.L. Su, *J. Mater. Chem.*, 2006, **11**, 663-677.
- Y. Lu, H. Fan, A. Stump, T.L. Ward, T. Rieker and C.J. Brinker, *Nature*, 1999, **398**, 223-226.
- N.M. Vinothan, I. Arnout, D.T. James and J.P. David, *Adv. Mater.*, 2001, **13**, 447-450.
- Y. Yang, G. Meng, X. Liu, L. Zhang, Z. Hu, C. He and Y. Hu, *J. Phys. Chem. C.*, 2008, **112**, 20126-20130.
- W. Qian, F. Sun, Y. Xu, L. Qiu, C. Liu, S. Wang and F. Yan, *Energy Environ. Sci.* 2014, **7**, 379-386.
- Y. Zhang, E.W. Shi, Z.Z. Chen, X.B. Li and B. Xiao, *J. Mater. Chem.*, 2006, **16**, 4141-4145.
- Z. Liu, L. Ci, N.Y. Jin-Phillipp and M. Ruhle, *J. Phys. Chem. C.*, 2007, **111**, 12517-12521.

38. J.B. Casady and R.W. Johnson, *Solid-State Electron.*, 1996, **39**, 1409-1422.
39. K. Shimoda, J.S. Park, T. Hinoki and A. Kohyama, *Appl. Surf. Sci.* 2007, **253**, 9450-9456.
40. R. Liu, B. Liu, K. Zhang, M. Liu, Y. Shao and C. Tang, *J. Nucl. Mater.* 2014, **453**, 107-114.
41. M. Biswal, A. Banerjee, M. Deo and S. Ogale, *Energy Environ. Sci.* 2013, **6**, 1249-1259.
42. M. J. Kim, Y. S. Hwang and J. H. Kim, *J. Power Sources*, 2013, **239**, 225-233.
43. M. J. Kim, Y. S. Hwang and J. H. Kim, *Phys. Chem. Chem. Phys.* 2014, **16**, 351-361.
44. J. Yan, Z. Fan, T. Wei, W. Qian, M. Zhang and F. Wei, *Carbon*, 2010, **48**, 3825-3833.
45. M.D. Stoller, S.J. Park, Y. Zhu, J.H. An and R.S. Ruoff, *Nano Lett.*, 2008, **8**, 3498-3502.
46. M. J. Kim, Y. S. Hwang, K. C. Min and J. H. Kim, *Phys. Chem. Chem. Phys.* 2013, **15**, 15602-15611.
47. J. Lin, C. Zhang, Z. Yan, Y. Zhu, Z. Peng, R.H. Hauge, D. Natelson and J.M. Tour, *Nano Lett.*, 2013, **13**, 72-78.
48. Z. Fan, J. Yan, T. Wei, L. Zhi, G. Ning, T. Li and F. Wei, *Adv. Funct. Mater.*, 2011, **21**, 2366-2375.
49. Y. Gogotsi and P. Simon, *Science*, 2011, **334**, 917-918.
50. Z.S. Wu, W. Ren, D.W. Wang, F. Li, B. Liu and H.M. Cheng, *ACS nano*, 2010, **4**, 5835-5842.



Graphical Abstract
80x55mm (300 x 300 DPI)